nature geoscience

SUPPLEMENTARY INFORMATION

DOI: 10.1038/NGEO2418

Anomalously fast convergence of India and Eurasia caused by double subduction

Oliver Jagoutz[1], Leigh Royden[1], Adam Holt[2] and Thorsten Becker[2]
[1]Department of Earth, Atmospheric and Planetary Sciences, MIT, Cambridge, MA 01890
[2]Department of Earth Sciences, University of Southern California, Los Angeles, CA 90089

DOI: 10.1038/NGEO2418

Fast Analytical Subduction Technique (FAST): Description and Evaluation

e1. General overview

We use the approach of Royden and Husson (2006) to calculate the geometry of subducting slabs and how it evolves over time, the velocity of the lithospheric plates outside of the subduction zones, and all stresses acting on the surfaces of the slabs, on the base of the plates, and transmitted along the slabs and plates. However, we use improved approximations for viscous flow, especially on the large (regional) scale, and have added frictional stress-coupling between the slabs and overriding plates. We refer to this method as "FAST" (Fast Analytical Subduction Technique).

We calculate the forces related to slab buoyancy, lithostatic overburden, and viscous flow in the asthenosphere analytically, and apply these at the slab surfaces. The slabs are treated as thin viscous sheets and bending of the slab is calculated at each time-step using a standard finite difference method. The bending deformation of the slab is the only discretized numerical computation used besides simple numerical integration and differentiation of the analytically-computed stresses on the slab surfaces.

As implemented, FAST consists of five sets of calculations that are repeated at each time-step. We begin each time step with the velocities of the plates, the geometries of the slabs, and the velocity of each point along the slabs as computed during the previous time-step.

1) The first set of calculations at each time-step involves derivation of the large-scale flow of asthenosphere that is driven by imposing the velocities and geometries of multiple slabs and plates as computed in the previous time step (Fig A1). We approximate large-scale flow in the asthenosphere as a Hele-Shaw flow (e.g. Batchelor, 1970). From this, we derive an analytical expression for the stresses on the base of the plates and the stresses that provide boundary conditions on the local viscous flow (Fig. e1).

2) Second, we adjust the slab-parallel component of the down-going plate velocity in order to maintain the desired configuration of the surface plates. The exact criteria for resetting the velocities depend on the geometry of the slabs (i.e. how many, what subduction polarity, etc.). The way in which the velocities are adjusted at each time-step can be used for systems where the velocity of one or more plates is prescribed in advance, or for free subduction where no *a priori* velocities are prescribed and the net horizontal force on the entire system is maintained at zero (or some other desired value).

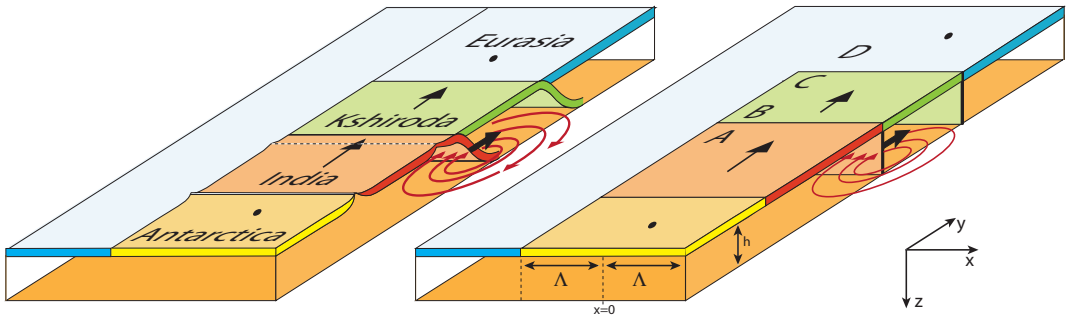

Figure e1. Slab and plate geometry used for calculations described in the main text and in this supplement. (Left) Geometry of the double subduction system as applied to the convergence of India and Eurasia. The dashed line shows the location of the extinct spreading ridge assumed to have existed north of India prior to 120 Ma. (Right). Red lines with arrows illustrate the phenomenon of toroidal flow of asthenosphere around the moving slab, which is approximated as a vertical boundary for computing the regional flow field.

3) We calculate and adjust the degree of plate coupling at lithospheric depths through a combination of topographic loading at the subduction boundary and a frictional criterion for shear coupling. In particular, we adjust the height and width of the topographic load above each subduction boundary and a coefficient of frictional sliding that acts between the overriding and down-going plates. For the geometry used in this paper, this adjustment acts to maintain zero net horizontal force on plate A and also on the combined plate B+C (Fig. e1). (The net vertical force on each plate is always zero.)

4) We derive the local viscous flow in the asthenospheric wedges above and below the slabs, and the associated stresses acting on the slabs (Fig. e2). This solution is embedded within the previously computed solution for large-scale viscous flow. In practice, only the viscous pressure to be applied to the open ends of the asthenospheric wedges, adjacent to the slabs, is needed to compute the local viscous flow and associated stresses on the slab. The method used is akin to that described for calculating local flow in Royden and Husson (2006) except that we use a slightly different analytical approximation for flow in the viscous wedges and include the additional stresses due to the local development of topography and frictional coupling between plates at lithospheric depths.

5) We derive the new slab geometry resulting from all sources of stress applied to the slabs. These include slab buoyancy, viscous pressure, viscous shear stress, frictional stress, and the pressure due to the overburden on the slab (Fig. e2). This is accomplished by solving the fourth-order ordinary differential equation for bending of a thin viscous or elastic sheet.

DOI: 10.1038/NGEO2418

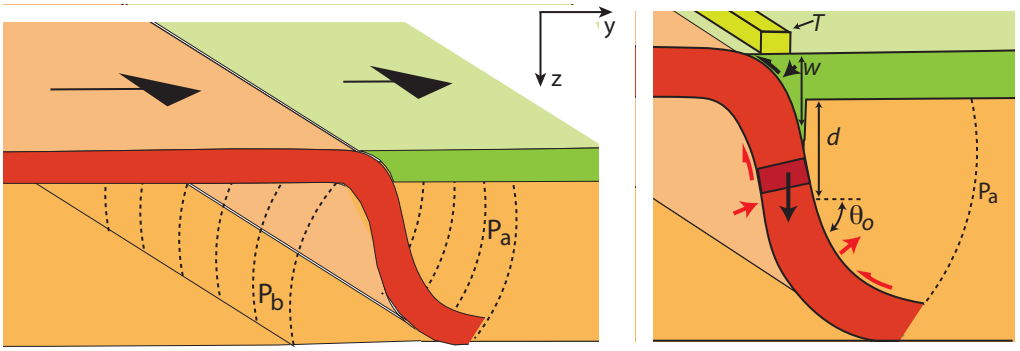

Figure e2. Slab geometry used for calculations described in this supplement. Left panel illustrates the location where pressure P_a and P_b, computed in the large-scale flow solution (supplement section e2), are applied to the local solution as boundary conditions. Right panel shows the location of the rectangular topographic load that adds to the normal and frictional shear stresses on the slab (supplement section e5). The orientation and sense of the stress due to static sources (normal stress and frictional shear stress at lithospheric depths and slab buoyancy) are shown in black, those due to viscous flow of the asthenospheric are shown in red.

This scheme yields a new set of velocities for all the plates, a new set of velocities for each point on the slabs, and a new value for the total horizontal component of force acting on each of plate elements in the system (these elements are plate A, plate B+C, and plate D in Fig. e1). These newly computed values are used to advance the model geometry to the next timestep. Each of these five steps is described in more detail in the following sections. At the end of this supplement, our results for double and single slab subduction are compared to those derived from the fully numerical, finite element software, CitcomCU, for a simple set of single and double subduction systems.

e2. Calculating large-scale viscous flow in the asthenosphere

We develop an analytical approximation for the large-scale flow and associated stresses that result from a series of subduction zones, spreading ridges and transform faults with a geometry similar to that shown in Fig. e1. Here, a series of parallel subduction boundaries (which may dip in either direction) and spreading ridges are assumed to have the same length along strike, equal to 2Λ. These plate boundaries are confined laterally by transform faults with the appropriate sense of motion. The plate velocities outside the transform faults are constrained to be uniform throughout each plate (the velocities of the side plates do not affect the results so long as there is only one side-plate on each side of the system of subduction boundaries).

For the purpose of approximating the large scale viscous flow, we treat each subduction boundary as a vertical plane extending from the surface to the base of the upper mantle (Fig. e1). Viscous flow at this scale is treated as a Hele-Shaw flow (Couette flow that is irrotational in the *x*-*y* plane, see Batchelor, 1970) with a uniform Newtonian viscosity, μ. The horizontal velocity at the base of the upper mantle is set to zero everywhere and all plate velocities, $\boldsymbol{v_p}$, are calculated relative to the top of the lower mantle (boldfaced symbols indicate vector quantities). If there are a total of J plates (not including the plates outside the transform boundaries), we designate each plate by an index j, and denote the velocity of each plate as $\boldsymbol{v_{pj}}$.

For Hele-Shaw flow, velocities in the asthenosphere are related to the lateral pressure gradient by:

$$\boldsymbol{V} = \boldsymbol{\nabla} P \left[\frac{(z^2 - zh)}{2\mu}\right] + \boldsymbol{v_p}\frac{(h - z)}{h} \qquad \text{e1}$$

where $\boldsymbol{V}$ and P are velocity and pressure, respectively. The vertically averaged flow velocity is then:

$$\overline{\boldsymbol{V}} = -\boldsymbol{\nabla} P \left(\frac{h^2}{12\mu}\right) + \frac{\boldsymbol{v_p}}{2}. \qquad \text{e2}$$

Conservation of mass (assuming an incompressible fluid) requires $\boldsymbol{\nabla} \cdot \overline{\boldsymbol{V}} = 0$, so that:

$$\nabla^2 P \left(\frac{h^2}{6\mu}\right) = \boldsymbol{\nabla} \cdot \boldsymbol{v_p}. \qquad \text{e3}$$

Solving for the large-scale viscous flow is equivalent to finding a solution for P that satisfies eq. (e3) everywhere except on the surfaces of the slabs; on each slab surface, P must satisfy eq. (e2) for $\overline{\boldsymbol{V}}$ equal to the horizontal velocity of that slab (relative to the top of the lower mantle). This can be accomplished using a variety of techniques. Here we choose a simple analytical solution that is applicable to the plate and slab geometries shown in Fig. e1.

For the plate system in Fig. e1, the plate velocities have only a y-component and the velocity is uniform over each plate. Let us denote the y-component of velocity of the jth plate as v_{pj} and let the location of the plate boundary (whether divergent or convergent) between plates $j - 1$ and j be located at $y = y_j$. The Laplacian of P is then given by:

e4

DOI: 10.1038/NGEO2418

$$\nabla^2 P\left(\frac{h^2}{6\mu}\right) = \begin{cases} \sum_{j=2}^{J} (v_j - v_{j-1})\delta(y - y_j) & |x| \le \Lambda \\ 0 & |x| > \Lambda \end{cases}$$

The solution for P that satisfies this equation is, to within an arbitrary constant:

$$P(x,y) = \sum_{j=1}^{J} A_j \left\{ (y - y_j)\left[\tan^{-1}\left(\frac{x-\Lambda}{y-y_j}\right) - \tan^{-1}\left(\frac{x+\Lambda}{y-y_j}\right)\right] + \left(\frac{x-\Lambda}{2}\right)\ln\left[(x-\Lambda)^2 + (y-y_j)^2\right] - \left(\frac{x+\Lambda}{2}\right)\ln\left[(x+\Lambda)^2 + (y-y_j)^2\right]\right\} \quad \text{e5}$$

where the coefficients A_j are:

$$A_j = \left(\frac{3\mu}{\pi h^2}\right)(v_{j-1} - v_j). \quad \text{e6}$$

The derivatives of pressure with respect to x and y are:

$$\frac{\partial P}{\partial x} = \sum_{j=1}^{J} \frac{A_j}{2}\left\{\ln\left[(x-\Lambda)^2 + (y-y_j)^2\right] - \ln\left[(x+\Lambda)^2 + (y-y_j)^2\right]\right\} \quad \text{e7}$$

$$\frac{\partial P}{\partial y} = \sum_{j=1}^{J} A_j \left[\tan^{-1}\left(\frac{x-\Lambda}{y-y_j}\right) - \tan^{-1}\left(\frac{x+\Lambda}{y-y_j}\right)\right] \quad \text{e8}$$

Combining eqs. (e2) and (e6-e8) yields the portion of the vertically-averaged velocity of the asthenosphere that is driven by the motion of the plates. We denote this velocity field as $\overline{\boldsymbol{V}}_{\boldsymbol{p}}$.

Fig. e3a shows the y-component of the vertically-averaged velocity that results from a single divergent or convergent boundary over the domain $|x| < \Lambda$ for several values of y. For all values of y, the magnitude of the y-component of velocity at $x = 0$ is fairly representative of its value over all $|x|$ between 0 and Λ, particularly for $|x| < \in 0.75\Lambda$. Thus, for ease of calculation, we use the vertically-averaged velocity at $x = 0$ as an approximation for the y-component of velocity over the entire interval $|x| < \Lambda$, for all values of y.

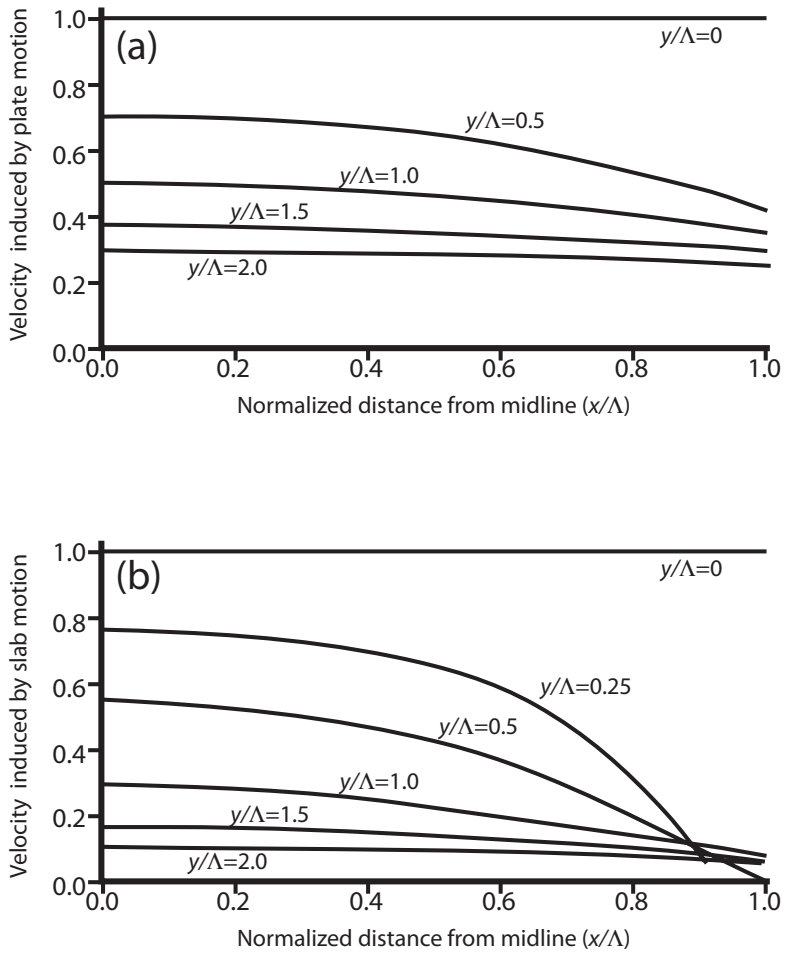

Figure e3. (a) The vertically-averaged velocity (y-component) that results from divergent or convergent motion of the overlying plates at a single plate boundary. Velocity is normalized to be one at the plate boundary. (b) The vertically-averaged velocity that results from motion of a single vertical slab. The velocity is normalized to be one at the plate boundary. x/Λ and y/Λ are normalized x- and y-components of distance from the center of the plate boundary using the coordinate system of Fig. e1.

DOI: 10.1038/NGEO2418

The next task is to determine the vertically averaged flow that is contributed to the system by the horizontal velocity of each slab, which we approximate as a vertical boundary extending from the surface to the base of the upper mantle (and which we will refer to as a "slab" for the remainder of this section, Fig. e1). For K subduction systems, we can denote the velocity of the k-th slab relative to the top of the lower mantle as $\overline{\boldsymbol{V}}_{\boldsymbol{k}}$. We define a residual velocity for each slab:

$$\overline{\boldsymbol{V}}_{\boldsymbol{Rk}} = \overline{\boldsymbol{V}}_{\boldsymbol{k}} - \overline{\boldsymbol{V}}_{\boldsymbol{pk}} \tag{e9}$$

where $\overline{\boldsymbol{V}}_{\boldsymbol{pk}}$ is the vertically-averaged velocity induced by the motion of the plates, as measured in the center of the k-th slab.

We seek a velocity field that matches $\overline{\boldsymbol{V}}_{\boldsymbol{Rk}}$ at each of K slabs and that satisfies $\nabla^2 P = 0$ elsewhere else. This is best accomplished in an elliptical coordinate system:

$$x = \Lambda \cosh(\lambda_k)\cos(\sigma_k), \tag{e10}$$

$$(y - y_k) = \Lambda \sinh(\lambda_k)\sin(\sigma_k) \tag{e11}$$

with σ_k between -π and π and λ_k between 0 and +∞. We choose P_k to be of the form:

$$P_k = \sum_{n=1}^{\infty} \Lambda B_{kn} \mathrm{e}^{-n\lambda_k} \sin(n\sigma_k) \tag{e12}$$

where the B_{kn} are coefficients to be determined. This expression satisfies $\nabla^2 P = 0$ everywhere except at $\lambda_k = 0$, which corresponds to the surface of the slab.

We can prescribe any desired y-component of velocity on a single slab by setting $\lambda_k = 0$, taking the appropriate derivatives, and using Fourier decomposition to solve for velocity. Although it is easiest to carry out calculations in elliptical coordinates, we use Cartesian coordinates for the sake of presentation, where we invert to find:

$$\cos^2(\sigma_k) = \frac{1}{2\Lambda^2}\left\{[\Lambda^2 + x^2 + (y - y_k)^2] - \sqrt{(\Lambda^2 + x^2 + (y - y_k)^2)^2 - 4\Lambda^2 x^2}\right\} \tag{e13}$$

$$\sin^2(\sigma_k) = \frac{1}{2\Lambda^2}\left\{[\Lambda^2 - x^2 - (y - y_k)^2] + \sqrt{(\Lambda^2 + x^2 + (y - y_k)^2)^2 - 4\Lambda^2 x^2}\right\} \tag{e14}$$

$$\cosh^2(\lambda_k) = \frac{1}{2\Lambda^2}\left\{[\Lambda^2 + x^2 + (y - y_k)^2] + \sqrt{(\Lambda^2 + x^2 + (y - y_k)^2)^2 - 4\Lambda^2 x^2}\right\} \tag{e15}$$

$$\sinh^2(\lambda_k) = \frac{1}{2\Lambda^2}\left\{[-\Lambda^2 + x^2 + (y - y_k)^2] + \sqrt{(\Lambda^2 + x^2 + (y - y_k)^2)^2 - 4\Lambda^2 x^2}\right\} \tag{e16}$$

The general expression for the pressure that results from imposing a uniform velocity on a single slab surface can be obtained by substituting eqs. (e13 – e16) into eq. (e12). This expression is lengthy in Cartesian coordinates and we omit it here. The corresponding y-component of the vertically-averaged velocity can be obtained by differentiating the resulting expression and substituting into:

$$\overline{V}_s = -\sum_{k=1}^{K} \frac{\partial P_k}{\partial y} \left(\frac{h^2}{12\mu} \right) \qquad \text{e17}$$

where the lack of boldface indicates the y-component of velocity.

The solution that, for a single slab, yields a uniform velocity across the slab occurs when all coefficients are zero except for $n = 1$. By inspection of eq. (e12), the $n = 1$ solution produces a step-change in pressure across the slab that is greatest at the midpoint of the slab ($x = 0$), zero at the edge of the slab ($x = \Lambda$), and varies as $\sin(\pi x)$. The subduction velocity of the slab (as calculated in section e6) is highly sensitive to this step-change in pressure across the slab, which is used as a boundary condition for calculating the local viscous stresses (section e5). Because the pressure in the center of a slab is more important in driving viscous flow than that near the edge of the slab, we use the viscous pressure computed at $x = 0$ as the boundary condition for integration of eq. (e29), which is derived later in this supplementary section. Arguably, one might wish to use the average pressure across the slab instead, which is $(2/\pi)$ times the pressure at $x = 0$.

Fig. e3b shows the y-component of the vertically-averaged velocity that results from solutions to eqs. (e12) and (e17) for $n = 1$. For all values of y, the magnitude of the y-component of the vertically-averaged velocity at $x = 0$ is representative of its value for $|x|$ between 0 and 0.75Λ, especially for $(y - y_k) > \Lambda/2$. For ease of calculation, we again use the vertically-averaged velocity at $x = 0$ as representative of the y-component of velocity over the interval $|x| < \Lambda$, for all values of y.

Considering only velocities that lie along the midline of the slabs and the plates, we can write the greatly simplified expression for pressure at $x = 0$:

$$P_k(0, y) = B_k \left(\sqrt{\Lambda^2 + (y - y_k)^2} - |y - y_k| \right) \left(\frac{|y - y_k|}{(y - y_k)} \right). \qquad \text{e18}$$

(Note that this has a step change value across the slab at $y = y_k$). Taking the corresponding derivative with respect to y yields:

$$\left. \frac{\partial P_k}{\partial y} \right|_{x=0} = B_k \left(\frac{|y - y_k|}{\sqrt{\Lambda^2 + (y - y_k)^2}} - 1 \right). \qquad \text{e19}$$

DOI: 10.1038/NGEO2418

Lastly, the vertically-averaged y-component of velocity that results from the motion of all K slabs, calculated along the midline at $x = 0$, is:

$$\overline{V}_s(0,y) = \sum_{k=1}^{K} B_k \left(\frac{h^2}{12\mu}\right)\left[\frac{|y-y_k|}{\sqrt{\Lambda^2+(y-y_k)^2}} - 1\right]. \qquad \text{e20}$$

The coefficients B_k are obtained by setting $\overline{V}_s$ equal to $\overline{V}_{Rk}$ at the position of all K slabs:

$$\overline{V}_{k'} = \overline{V}_{pk'} + \overline{V}_s(0,y_{k'}) = \overline{V}_{pk} + \sum_{k=1}^{K} B_k \left(\frac{h^2}{12\mu}\right)\left(\frac{|y_{k'}-y_k|}{\sqrt{\Lambda^2+(y_{k'}-y_k)^2}} - 1\right) \qquad \text{e21}$$

where the lack of boldface indicates the y-component of velocity. The appropriate values of B_k can be found by matrix inversion for multiple slabs (and are trivial to calculate for one or two slab systems such as those considered in this paper).

Once the B_k are obtained, the vertically-averaged velocity and the pressure at any point in the system can be found by combining the foregoing equations. Along the midline of the slab, the total pressure from all sources is:

$$\begin{aligned} P(0,y) = &\sum_{j=1}^{J} A_j \left\{\left[-2(y-y_j)\tan^{-1}\left(\frac{\Lambda}{y-y_j}\right)\right] - \Lambda \ln\left[\Lambda^2+(y-y_j)^2\right]\right\} \\ &+ \sum_{k=1}^{K} B_k \left(\sqrt{\Lambda^2+(y-y_k)^2} - |y-y_k|\right)\left(\frac{|y-y_k|}{(y-y_k)}\right). \end{aligned} \qquad \text{e22}$$

Eq. (e22) gives the total pressure field into which we imbed our solution for the local viscous flow in the mantle wedges above and below the slab.

In choosing the precise pressure boundary conditions for the open ends of the mantle wedges above and below slab k, we identify the points where, (a), the slab descends beneath the overriding lithosphere (typically 80-100 km depth) and, (b), the end of the slab where it nears the base of the upper mantle (Figs. e1 and e2; see also Royden and Husson, 2006, for discussion of how the slab end is defined). The location of y_k is defined at the midway point between (a) and (b). The pressure that is used as a boundary condition for the open end of the mantle wedge above the slab is that calculated at location (a); the pressure that is used as a boundary condition for the open end of mantle wedge below the slab is the pressure calculated at location (b). In general, it is only the pressure difference between (a) and (b) that is significant.

Outside of each subduction boundary, the y-compnent of shear stress on the base of each plate, integrated from positions y_1 to y_2, is:

$$\int_{y_1}^{y_2} \tau_{yz} dx = \frac{P(y_1) - P(y_2)}{2} + \frac{v_p \mu}{h}(y_1 - y_2). \qquad \text{e23}$$

e3. Adjustment of slab-parallel velocities

For the two-slab system used in this paper, we are concerned with a coupled system of two synthetic (i.e. dipping in the same direction) subduction boundaries. The plate that corresponds to Eurasia (plate D in Fig. e1) needs to be held fixed with respect to the top of the lower mantle at all times. The velocities of the intermediate plates, between the two subduction boundaries (plates B and C), need to be kept equal, effectively merging them into a single plate, BC. The magnitude and sign of their joint velocity is not known *a priori*.

In the method used to calculate the bending deformation of each slab (described in section e6), we cannot prescribe the velocities of the overriding (non-subducting) plates. Instead, we calculate the new slab geometry and the velocity of the overriding plate simultaneously from a set of criteria that include the slab-parallel velocity of the down-going plate. Thus, for the two-plate system described in this paper, we can only specify the velocities of plates A and plate C at each time step.

In order to maintain the desired velocities of plates B (equal to that of plate C) and D (equal to zero) we must adjust the slab-parallel component of velocity for plates A and C appropriately at each time-step. For example, for the plate system used in this paper, if the computed velocity of plate D is greater than zero in the previous time-step, we adjust the slab-parallel velocity of plate C downward; if the computed velocity of plate D is greater than zero in the previous time-step, we adjust the slab-parallel velocity of plate C upward. Typically we adjust the velocity by 1/4 or 1/8 of the difference between the computed and the desired velocity of plate B at each time-step. We perform a similar adjustment for plate A velocities to keep the velocity of plates B and C equal.

We can adopt a similar procedure when the subduction system is “free”, i.e. there are no prescribed velocities on any plate in the system. In this case, we wish to keep the net horizontal force on the entire system equal to zero. By way of example, in a system with a single subduction boundary, we would derive the pressure that acts on both sides of the vertical slab boundary and the shear stresses that act on the base of both plates from our regional-scale calculations (section e2). We then sum the pressure on each vertical “slab” surface, multiplied by the height of this vertical “ slab”, and the shear stress integrated over the base of both plates. If this sum is greater than zero, we decrease the velocity of the foreland lithosphere going into the next time-step (typically by 1 mm/yr for each .01 m.y. timestep) or *vice versa*. This method of force balance was not needed in this paper because the velocity of the Eurasian plate (D) was fixed at zero regardless of the net horizontal force acting on it.

DOI: 10.1038/NGEO2418

e4. Plate coupling

We adjust the degree of plate coupling at lithospheric depths through a combination of topographic loading at each subduction boundary and a frictional criterion for shear coupling. An increase in topographic elevation over the down-going slab is applied as an additional normal stress on the subducting plate. This additional normal stress is $T(\rho_c-\rho_w)g$ whenever the "topography" is below sea level and $T\rho_c g$ for topography above sea level. (T is topography, ρ_c is crustal density, ρ_w is water density and g is acceleration due to gravity.) The topographic load is applied over a specified width and extends from the position where the down-going plate passes beneath the overriding plate toward the trench. Shear stress is set equal to a coefficient λ times the normal stress acting at each point along the plate interface.

The goal of this exercise is to maintain zero net horizontal force on plate A and on the combined plate BC. At each time-step, the topographic load and the coefficient of shear coupling are adjusted independently for each subduction boundary in order to maintain the desired force balance.

We begin at time zero with no topographic load and a frictional shear coefficient λ=0.3. Subsequently, if the net horizontal force acting on plate A is computed to be less than zero in the previous time-step, we adjust the topographic elevation, the width of the topographic load and the coefficient of shear coupling upwards for the next time-step (typically by 50 m, 5 km, and .001 respectively). We do the opposite if the net horizontal force acting on plate A is computed to be greater than zero in the previous time-step. We limit the width of the topographic load to a maximum of 400 km and constrain λ to be greater than or equal to zero. In this paper, during double subduction, the boundary between plates A and B (Trans-Tethyan subduction system) typically developed $T\approx$2.5 km with a width of ~250 km and $\lambda\approx$0.5. The boundary between plates C and D (Andean margin of southern Eurasia) typically developed $T\approx$4 km with a width of ~400 km and $\lambda\approx$0.8. Note that these are heights above the incoming sea floor, not height above sea-level.

e5. Calculating local viscous flow in the asthenospheric wedges

The system that we use for calculating viscous flow and stresses in the mantle wedges above and below the slab is similar to that described by Royden and Husson (2006) except that we use a uniform viscosity (instead of their more complex two-layer viscosity) and assume a slightly different mathematical form to approximate flow within the wedge. We treat the local viscous flow in the mantle wedges as invariant in the trench-parallel (x) direction, so that we need only concern ourselves only with flow in the y-z plane. This is a reasonable approximation provided we are not concerned with flow close to the lateral boundaries of the slabs and that the trench-parallel width of the slab is not too narrow (see Royden and Husson, 2006, for discussion).

Consider the stream function:

$$\psi = r[E\cos(\theta) + F\sin(\theta) + G\theta\cos(\theta) + H\theta\sin(\theta)]. \qquad \text{e24}$$

For constant *E*-*H*, this is the exact solution for viscous flow in an infinite, uniform-geometry wedge with uniform velocities applied along the radial boundaries of the wedge. To compute flow in the somewhat non-uniformly shaped viscous wedge that lies above the slab, we treat the upper surface of the wedge (defined as θ=0) as a horizontal boundary coincident with the base of the overriding plate (Fig. e2). The lower surface of the wedge is coincident with the upper surface of the slab and may be gently undulating; locally this we assign this surface a slope $\theta_o(r)$ where, if d is the vertical thickness of the wedge at any point, r is defined as $r=d\sin(\theta_o)$.

Because the lower surface of the wedge is not exactly planar and the velocities on that surface are not completely uniform, we allow the coefficients *E*-*H* to be functions of r but consider their derivatives with respect to r to be negligible. Neglecting all terms that involve differentiation of velocity with respect to r, we obtain:

$$v_\theta = \frac{\partial \psi}{\partial r} \qquad \text{e25}$$

$$v_r = -\frac{1}{r}\frac{\partial \psi}{\partial \theta} \qquad \text{e26}$$

$$\tau_{r\theta} \approx \mu\left(\frac{1}{r}\frac{\partial v_r}{\partial \theta} - \frac{v_\theta}{r}\right) \qquad \text{e27}$$

$$\tau_{rr} = -\tau_{\theta\theta} \approx 0 \qquad \text{e28}$$

$$\frac{\partial P}{\partial r} \approx \frac{1}{r}\frac{\partial \tau_{r\theta}}{\partial \theta}. \qquad \text{e29}$$

The boundary conditions that we apply at θ=0 are a uniform radial (horizontal) velocity, v_c, and zero tangential (vertical) velocity. The boundary conditions along the base of the wedge are a radial velocity v_r and a tangential velocity v_θ, both of which may vary along the lower surface of the wedge. For these boundary conditions and under the assumption that derivatives of *E*-*H* with respect to r are negligible, we obtain E=0 and:

DOI: 10.1038/NGEO2418

$$F = \frac{-v_c {\theta_o}^2 - v_{ro}\theta_o \sin(\theta_o) - \left(\frac{1}{r}\psi_o\right)[\sin(\theta_o) + \theta_o \cos(\theta_o)]}{{\theta_o}^2 - \sin^2(\theta_o)} \quad \text{e30}$$

$$G = \frac{v_c \sin^2(\theta_o) + v_{ro}\theta_o \sin(\theta_o) + \left(\frac{1}{r}\psi_o\right)[\sin(\theta_o) + \theta_o \cos(\theta_o)]}{{\theta_o}^2 - \sin^2(\theta_o)} \quad \text{e31}$$

$$H = \frac{v_c[\theta_o - \cos(\theta_o)\sin(\theta_o)] + v_{ro}[\sin(\theta_o) - \theta_o \cos(\theta_o)] + \left(\frac{1}{r}\psi_o\right)\theta_o \sin(\theta_o)}{{\theta_o}^2 - \sin^2(\theta_o)} \quad \text{e32}$$

where:

$$\psi_o = \int_{r_o}^{r} v_{\theta o}\, \partial r. \quad \text{e33}$$

The corresponding velocities, shear stresses and $\partial P/\partial r$ on the upper and lower boundaries of the wedge can be found by substituting these expressions into eqs. (e25-e29). The viscous pressure on the slab can be found by requiring that the viscous pressure at the open end of the wedge be equal to that obtained from the calculation of large-scale flow (section e2 and Figs. e1 and e2), and by integration of eq. (e29) over r. An equivalent calculation can be made for the mantle wedge beneath the slab.

The shear stress and the normal stress due to viscous flow in the wedge vary approximately as $1/d$, being largest (in magnitude) at the narrow end of the wedge. The termination of the viscous wedge at its narrow end is described by Royden and Husson (2006), and is the region where the pressure required to flux asthenosphere into and the narrow end of the wedge is equal to the lithostatic pressure at the back end of the static frontal wedge (Fig. e2). In essence, the applied pressure boundary conditions at the open end of the mantle wedge affect the local solution such that: when the pressure above the slab decreases, there is an increase in the upward force acting along the slab surface, inhibiting subduction, and *vice versa*. The converse is the case for the pressure boundary condition applied to the mantle wedge below the slab.

In this manner, the viscous pressures due to large-scale flow are carried into the local flow solutions and affect the pressure at every point on the slab. Embedded in the pressure boundary conditions on local flow are the effects of the large-scale geometries and velocities of all plates and slabs. Thus the local flow calculations are always conducted within the stress field generated by the large-scale flow.

e6. Calculating flexural bending of the slab

In the last step we compute the flexural bending of the slab in response to all the applied loads. The slab is not allowed to stretch in a direction parallel to the down-dip direction. We use a thin-sheet approximation for bending of a viscous slab that is correct for all slab dips (unlike the standard expression for flexural bending, which is a small-angle approximation). We choose to use a variable, $\mathcal{H}$, defined as:

$$\mathcal{H}(s) = \int_s^\infty \theta_o \, \partial s \qquad \text{e34}$$

where s is the up-dip distance from the end of the slab. Although closely related to the vertical deflection of the slab, $\mathcal{H}$ has the advantage that it is numerically more tractable at dips near vertical. H has units of length and, where the slab dip is small, is effectively equal to the vertical deflection of the slab through the small angle approximation for $\sin(\theta_o)$.

The flexural equation for bending of a thin viscous sheet is:

$$\frac{\partial^2}{\partial s^2}\left(D_v \frac{\partial^2 \dot{\mathcal{H}}}{\partial s^2}\right) + c(s)\frac{\partial^2 \mathcal{H}}{\partial s^2} = \sum_{\substack{\text{all} \\ \text{sources}}} \sigma_n(s) \qquad \text{e35}$$

where D_v is the viscous flexural rigidity of the slab and $\dot{\mathcal{H}}$ indicates the derivative of $\mathcal{H}$ with respect to time. The σ_n are the normal stresses, including the appropriate component of slab buoyancy, that act on the slab at s, and $c(s)$ is the compressional force along the slab. D_v is related to the slab viscosity, μ_s, and slab thickness, L, by:

$$D_v = \frac{L^3}{12\mu_s} \qquad \text{e36}$$

and $c(s)$ can be computed from:

$$c(s) = \cos(\theta_o)\int_0^s \sigma_x(s)\,\partial s - \sin(\theta_o)\int_0^s \sigma_z(s)\,\partial s \qquad \text{e37}$$

where σ_x and σ_z are the horizontal and vertical (including slab buoyancy) components of stress on the slab.

DOI: 10.1038/NGEO2418

Eq. (e35) is not stable for numerical solution by finite differences. We define σ_{vn} as the viscous stresses that act normal to the upper and lower surface of the slab. We also define ρ_{in} as the density of infilling material above the subducting plate in each location; it is equal to the density of the asthenosphere, ρ_a, where the subducting plate is overlain directly by asthenosphere. Letting $\Delta\rho = (\rho_a - \rho_{in})$, and noting that $c(s)$ is generally negative, we transform (e35) for negative σ_{vn}:

$$\frac{\partial^2}{\partial s^2}\left(D_v \frac{\partial^2 \dot{\mathcal{H}}}{\partial s^2}\right) + c(s)\Delta t \frac{\partial^2 \dot{\mathcal{H}}}{\partial s^2} + \left[\frac{|\sigma_{vn}|}{\dot{H}_{old}} + \frac{\Delta\dot{\rho} g w_{old}}{\mathcal{H}_{old}}\right]\dot{\mathcal{H}} =$$
$$-c(s)\frac{\partial^2 \mathcal{H}_{old}}{\partial s^2} + |\sigma_{vn}| + \left[\frac{\Delta\rho g w_{old}}{\mathcal{H}_{old}}\right]\dot{H}_{old} + \sum_{\substack{\text{all}\\ \text{sources}}} \sigma_n(s) \qquad \text{e38}$$

where the subscript "old" refers to values from the previous timestep. We solve this differential equation for $\dot{\mathcal{H}}$ through a decomposition technique for inverting 5-band matrices.

Written in Fortran and compiled, this technique typically produces 3D subduction results in a matter of seconds on a typical laptop computer. Results for the two-slab case shown in Supplement B were computed in approximately one second, while results for the Himalayan case computed in the main text were computed in approximately 15 seconds.

e7: Evaluating the Fast Analytical Subduction Technique (FAST)

A complete evaluation of the subduction model presented here is beyond the scope of this supplementary section, but we include a short section comparing semi-analytical model results of FAST to those generated by the fully numerical code CitcomCU for single and double subduction, section B1. All parameters used in FAST in this supplementary section are identical to those used to generate the results in the main text, except for plate length and width and slab buoyancy, and are given in Table e1. In particular, the viscosity and density of the asthenosphere, the thickness and viscosity of the lithosphere, and the loading and plate loading and coupling mechanisms are identical, with the identical parameter values.

The finite-element code CitcomCU (Moresi & Gurnis, 1996; Zhong, 2006) solves the equations governing convection in an incompressible viscous fluid without inertia, in the Boussinesq approximation, and, in our case, zero internal heating. In this section, subduction is modeled in a 3-D box with a dimensional height of 660 km, length of 5280 km, and width of 5280 km (symmetry about the midline allows a width of 2640 km to be used for the computations). The lithospheric plates have an initial uniform thickness of 80 km and uniform initial temperature of 273 K. The lithosphere is initially 85 kg/m^3 denser, and a factor of 500 more viscous than the surrounding mantle, which has a density and

viscosity of 3300 kg/m^3 and $1.4 \cdot 10^{20}$ Pa s. Density is a linear function of temperature, and viscosity has a Frank-Kamenetskii (1969) temperature dependence.

Subduction is initiated by prescribing an asymmetric lithospheric geometry in the trench region of the subducting plate, in the form of a quarter-circle notch, which extends to a depth, and has a radius of curvature, of 150 km (e.g. Enns et al., 2005). To decouple the subducting plates from the upper plates, we insert a 15 km thick, weak crustal layer within the subducting plate (e.g. Běhounková & Čížková, 2008). The crust extends along the length of the subducting plates and has a constant viscosity of half that of the mantle, and no additional density component. The crust is defined using compositional tracers, which are advected in the flow field. In order to accurately resolve the 15 km thick crust at the plate boundaries, we locally refine the fixed mesh: In close proximity to plate boundaries, elements have dimensions of 6.5 km and elsewhere they are 13 km wide. 40 compositional markers are initially contained within each of the elements. Regarding boundary conditions, the upper boundary has a constant temperature of 273 K and the base and sides have zero heat flux. Mechanically, all boundaries are free slip.

The geometry used for comparison between CitcomCU and FAST is identical to that shown in Fig. e1, and consists of lithospheric plates with a trench-parallel width of 2000 km (and side plates) with a total, trench-perpendicular plate length is 3960 km. Three subduction geometries were analysed. First, a double subduction system where all three plates are 1320 km in length and both slabs dip in the same direction. Second, a single plate subducting in two geometric configurations, but with an equivalent total plate length of 3960 km: a), a short subducting plate (1320 km) beneath a long overriding plate (2640 km) and, b), a long plate (2640 km) subducting beneath a short plate (1320 km).

In comparing FAST to CitcomCU, we matched as many parameters as possible. Plate thickness, buoyancy, viscosity, and the density of the mantle and of the asthenosphere were identical. However, there are differences between the two models that cannot be easily removed. These include differences in the normal and shear stress conditions used in plate coupling; FAST uses a frictional stress criteria with the development of topography while CitcomCU uses a weak viscous interface. In FAST, the plates are not allowed to stretch in a down-dip direction, while there is significant stretching of slabs and plates in the numerical model results. In CitcomCU, the deep end of the slab remains at the base of the upper mantle following subduction while it is removed from the model in FAST. Lastly, FAST is not specifically designed for situations where the slab does not extend to the base of the upper mantle because the large-scale flow calculations assume that asthenosphere cannot flow under the end of the slab. Nevertheless, we show results from FAST from times before the slab end reaches the base of the upper mantle.

DOI: 10.1038/NGEO2418

Despite the differences between various aspects mechanical aspects of the semi-analytical and numerical models, the results of both models are very similar for all three subduction geometries (Fig. e4). Most importantly, the absolute and relative plate velocities are very similar for all three subduction geometries after the ends of all slabs have reached the base of the upper mantle (after about 6 m.y.). Surprisingly, the "ramp up" portion of the subduction process, before the slabs reach the base of the upper mantle, were also in good agreement. Experimentation with the semi-analytic modeling indicates that many of the small differences in rates between the two models can be attributed to plate stretching in the numerical modeling runs.

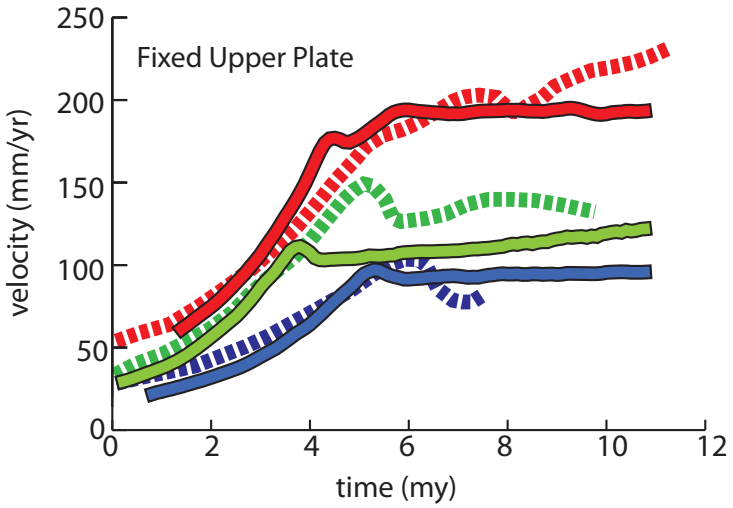

Figure e4. Comparison of CitcomCU (dashed lines) and FAST (solid lines) for single subduction (green and blue lines) and double subduction (red lines) systems, the latter with the geometry shown in Fig. e1. The double subduction system is initiated with three plates of length 1320 km while the single subduction systems are initiated with a downgoing plate length of 1320 km and an overriding plate length of 2640 km (green lines) or a downgoing plate length of 2640 km and an overriding plate length of 1320 km (blue lines).

Table e1. Values and Parameters Used in FAST Subduction Calculations in Main Text

Time step	10,000 yrs
Node spacing	5 km
Depth to base of upper mantle	660 km
Asthenosphere viscosity	$1.4 \cdot 10^{20}$ Pa s
Slab viscosity	$7.0 \cdot 10^{22}$ Pa s
Lithospheric thickness	80 km
Asthenosphere density	3300 kg/m^3
Static frontal wedge, infilling density	3000 kg/m^3
Initial coefficient of friction at plate interface[1]	0.3
Slab width (trench parallel) before 85 Ma	10,000 km
Slab width (trench parallel) after 70 Ma	3000 km
Buoyancy of old oceanic lithosphere, equivalent water depth	6000 m
Buoyancy of oceanic lithosphere with age, equivalent water depth[2]	$2500\ \mathrm{m} + 350\ \mathrm{m}\sqrt{\mathrm{age\ (m.y.)}}$
Buoyancy, continent, equivalent water depth	0 m
Kshiroda plus Indian plate lengths at 120 Ma	9300 km
Indian plate length at 120 Ma[3]	5900 km
Indian plate, oceanic part, (neo-Tethys) length at 120 Ma[3]	2400 km
Indian passive margin length (north side)[4]	500 km
Indian continent length (without northern passive margin)	3000 km
Indian plate oceanic (Neo-Tethys) depth at 120 Ma[5]	40 mm/yr spreading at ridge
Kshiroda plate length at 120 Ma[5]	3150 km
Kshiroda plate water depth (all times)	6 km
Kohistan arc width	250 km

[1]varies through time reaching ~.05 for the southern system and ~.08 for the northern subduction system
[2]not to exceed 6 km depth
[3]not including lithosphere that has already entered the subduction systems
[4]buoyancy varies linearly with distance across the margin
[5]full spreading rate; ridge located 1800 km north of the Indian margin; spreading ends at 120 Ma

References for Supplementary Material

Batchelor, G.K., 1967, An Introduction to Fluid Dynamics, Cambridge University Press, 366 pp.

Běhounková, M. and Čížková, H., 2008. Long-wavelength character of subducted slabs in the lower mantle, Earth Planet. Sci. Lett., 275, 43–53.

Enns, A., Becker, T. W., and Schmeling, H., 2005. The dynamics of subduction and trench migration for viscosity stratification, Geophys. J. Int., 160, 761–775.

DOI: 10.1038/NGEO2418

Frank-Kamenetskii, D. A., 1969. in Diffusion and Heat Transfer in Chemical Kinetics, p. 574, Plenum, New York.

Moresi, L. N. and Gurnis, M., 1996. Constraints on the lateral strength of slabs from three-dimensional dynamic flow models, Earth Planet. Sci. Lett., 138, 15–28.

Morgan, W.J. and Morgan, J.W., 2007, Plate velocities in the hotspot reference frame, GSA Spec. Papers, 430, 65-78.

Royden, L.H. and Husson, L., 2006, Trench motion, slab geometry and viscous stresses in subduction systems, Geophys. J. Int., 167, 881–905.

Zhong, S., 2006. Constraints on thermochemical convection of the mantle from plume heat flux, plume excess temperature and upper mantle temperature, J. Geophys. Res., 111(B04409), doi: 10.1029/2005JB003972.